



1

2 Estimation of Liquid Water Path in Stratiform Precipitation Systems using Radar Measurements

3 during MC3E

4

5 Jingjing Tian¹, Xiquan Dong¹, Baike Xi¹, Christopher R. Williams², and Peng Wu¹

6

7 ¹Department of Hydrology and Atmospheric Sciences, University of Arizona, Tucson, Arizona,

8 USA

9 ² Department of Ann and H.J. Smead Aerospace Engineering Sciences, University of Colorado

10 Boulder

11

12

13 Manuscript Submitted to Atmospheric Measurement Techniques

14

15

16 Corresponding author address: Dr. Xiquan Dong, The Department of Hydrology and

17 Atmospheric Sciences, University of Arizona, 1133 E. James Rogers Way, Tucson, AZ 85721-

18 0011.

19 Email: xdong@email.arizona.edu; Phone: 520-621-4652

20



21 **Abstract**

22 In this study, the liquid water path (LWP) in stratiform precipitation systems is retrieved, which
23 is a combination of rain liquid water path (RLWP) and cloud liquid water path (CLWP). The
24 retrieval algorithm uses measurements from the vertically pointing radars (VPRs) at 35 GHz and
25 3 GHz operated by the U.S Department of Energy Atmospheric Radiation Measurement (ARM)
26 and National Oceanic and Atmospheric Administration (NOAA) during the field campaign
27 Midlatitude Continental Convective Clouds Experiment (MC3E). The measured radar
28 reflectivity and mean Doppler velocity from both VPRs and spectrum width from the 35 GHz
29 radar are utilized. With the aid of the cloud base detected by ceilometer, the LWP in the liquid
30 layer is retrieved under two different situations: (I) no cloud exists below the melting base, and
31 (II) cloud exists below the melting base. In (I), LWP is primarily contributed from raindrops
32 only, i.e., RLWP, which is estimated by analyzing the Doppler velocity differences between two
33 VPRs. In (II), cloud particles and raindrops coexist below the melting base. The CLWP is
34 estimated using a modified attenuation-based algorithm. Two stratiform precipitation cases (20
35 May 2011 and 11 May 2011) during MC3E are illustrated for two situations, respectively. With
36 a total of 14 hours of samples during MC3E, statistical results show that the occurrence of cloud
37 particles below the melting base is low (8%), however, the mean CLWP value can be up to 0.87
38 kg m^{-2} , which is much larger than the RLWP (0.22 kg m^{-2}). When only raindrops exist below the
39 melting base, the averaged RLWP value is larger (0.33 kg m^{-2}) than the with cloud situation. The
40 overall mean LWP below the melting base is 0.39 kg m^{-2} for stratiform systems during MC3E.

41



42

43 **1. Introduction**

44 Clouds in stratiform precipitation systems are important to the Earth's radiation budget.
45 The vertical distributions of cloud microphysics, ice and liquid water content (IWC/LWC),
46 determine the surface and top-of-the-atmosphere radiation budget and redistribute energy in the
47 atmosphere (Feng et al., 2011; 2018). Also, stratiform precipitation systems are responsible for
48 most tropical and midlatitude precipitation during summer (Xu, 2013). However, the
49 representation of those systems in global climate and cloud-resolving models are still challenging
50 (Fan et al., 2015). One of the challenges is due to the lack of comprehensive observations and
51 retrievals of cloud microphysics (e.g. prognostic variables IWC and LWC) in stratiform
52 precipitation systems. Liquid water path (LWP), defined as an integral of LWC in the
53 atmosphere. It is a parameter used to provide the characterization of liquid hydrometeors in the
54 vertical column of atmosphere and study clouds and precipitation. The estimation of LWC/LWP
55 is one of the critical objectives of the US Department of Energy's (DOE) Atmospheric Radiation
56 Measurement (ARM) Program (Ackerman and Stokes, 2003).

57 LWP can be retrieved using the ground-based MicroWave Radiometer (MWR) sensed
58 downwelling radiant energy at 23.8 and 31.4 GHz (Liljegren et al., 2001). In last two decades,
59 ARM has been operating a network of 2-channel (23.8- and 31.4-GHz) ground-based MWR to
60 provide a time series of LWP at the ARM Southern Great Plains (SGP) site (Cadeddu et al.,
61 2013). Absorption-based algorithms using multichannels of MWRs have been widely used to
62 retrieve cloud LWP (e.g., Liljegren et al. 2001; Turner, 2007), and it is known to be accurate
63 methods to estimate LWP of nonprecipitating clouds with mean LWP error of 15 g m^{-2} (Crewell
64 and Löhnert, 2003). However, in precipitating conditions, LWP retrieved from conventional



65 MWR are generally not valid due to the violation of the Rayleigh assumption when large
66 raindrops exist (e.g., Saavedra et al., 2012). In addition, large increase of brightness
67 temperatures is measured as a result of the deposition of raindrops on the MWR's radome.
68 Unfortunately, it is very hard to model and quantify this increase from rain layer on the radome
69 (Cadeddu et al., 2017). This "wet-radome" issue largely inhibits the retrieving of LWPs using
70 ground-based MWR during precipitation. Due to the limitations of retrieving LWP from MWR
71 during precipitation, cloud and precipitation radars were used to simultaneously retrieve LWP
72 (Matrosov, 2010).

73 In the precipitating system, the liquid water cloud droplets and raindrops often coexist in
74 the same atmospheric layer (e.g., Dubrovina, 1982; Mazin, 1989; Matrosov, 2009, 2010),
75 indicating that the LWP consists of both cloud liquid water path (CLWP) and rain liquid water
76 path (RLWP). However, the discrimination between suspended small cloud liquid water droplets
77 and precipitating large raindrops is a very challenging remote sensing problem. Even though the
78 partitioning of LWP into CLWP and RLWP is important in cloud modeling (Wentz and Spencer,
79 1998; Hillburn and Wentz, 2008), there are few studies retrieved RLWP and CLWP
80 simultaneously and separately (Saavedra et al., 2012; Cadeddu et al., 2017). Battaglia et al.
81 (2009) developed an algorithm to retrieve RLWP and CLWP from the six Advanced Microwave
82 Radiometer for Rain Identification (ADMIRARI) observables under rainy conditions. Saavedra
83 et al (2012) developed an algorithm using both ADMIRARI and a micro rain radar to retrieve
84 and analyze the CLWP and RLWP for midlatitude precipitation during fall. In addition to these
85 RLWP and CLWP estimations mainly from passive microwave radiometers, there are several
86 studies to estimate the LWP using active radar measurements only. Ellis and Vivekanandan
87 (2011) developed an attenuation-based technique to estimate LWC, which is the sum of cloud



88 water contents (CLWC) and rain liquid water contents (RLWC), using simultaneous S- and Ka-
89 band scanning radars measurements. However, it is not always applicable of using these
90 techniques to retrieve LWC. If raindrop diameters are comparable to at least one of the radars'
91 wavelength, "Mie effect" will be included in the measured differential reflectivity, however this
92 "Mie effect" is not very distinguishable from differential attenuation effects (Tridon et al., 2013;
93 Tridon and Battaglia 2015).

94 Matrosov (2009) developed an algorithm to simultaneously retrieve CLWP and layer-
95 mean rain rate using the radar reflectivity measurements from three ground-based W-, Ka-, S-
96 bands radars. The CLWP were retrieved based on estimating the attenuation of cloud radar
97 signals compared to S-band radar measurements. Matrosov (2010) developed an algorithm to
98 estimate CLWP using a vertical pointing Ka-band radar and a nearby scanning C-band radar.
99 The layer-mean rain rate was first estimated with the aid of surface disdrometer, and then CLWP
100 was retrieved by subtracting the rain attenuation from total attenuation measured from two radars.
101 For the estimation of RLWP, Williams et al. (2016) developed a retrieval algorithm for rain drop
102 size distribution (DSD) using doppler spectrum moments observed from two collocated vertical
103 pointing radar (VPRs) at frequencies of 3 GHz and 35 GHz. The retrieved air motion and DSD
104 parameters were evaluated using the retrievals from a collocated 448-MHz VPR.

105 In this study, the CLWP retrieval algorithms in Matrosov (2009 and 2010) have been
106 modified given the available radar measurements, vertical pointing Ka- and S-band radars,
107 during the Midlatitude Continental Convective Clouds Experiment (MC3E) field campaign. For
108 the estimation of RLWP, we will basically follow the idea described in Williams et al. (2016) to
109 retrieve microphysical properties for raindrops, however instead of retrieving vertical air motion
110 and rain DSDs (Williams et al., 2016), this study aims at retrieving RLWCs, and then integrating



111 RLWCs over the liquid layer to estimate RLWP. Overall, in this study, algorithms from three
112 former publications are modified and combined to estimate the LWP in the stratiform
113 precipitating systems.

114 The goals of this study are to retrieve the LWP, which includes both RLWP and CLWP
115 retrievals using radars measurements, and tentatively answer two questions based on
116 observations and retrievals in the stratiform precipitation systems during MC3E: (1) what is the
117 occurrence of cloud below the melting base in the stratiform precipitation systems; (2) what are
118 the values of simultaneous CLWP, RLWP and LWP, and how does CLWP or RLWP contribute
119 to the LWP. Note that the CLWP and RLWP are constrained in a stratiform precipitation layer
120 below the melting base and above the surface. The LWP estimations in this study are primarily
121 aimed at stratiform precipitating events exhibiting melting-layer features from radar
122 measurements with lower-to-moderate rain rates ($RR < 10 \text{ mm hr}^{-1}$). The instruments and data
123 used in this study are introduced in section 2. Section 3 describes the methods of retrieving LWP
124 (both RLWP and CLWP). Section 4 illustrates two examples and followed by statistical results
125 from more samples during MC3E. The last section gives the summary and conclusions.
126 Acronyms and abbreviations are listed in Table 1.

127

128 **2. Data**

129 The MC3E field campaign, co-sponsored by the NASA Global Precipitation
130 Measurement and the U.S. DOE ARM programs, was conducted at the ARM SGP (northern
131 Oklahoma) during April-June 2011 to study convective clouds and improve model
132 parametrization (Jensen et al., 2015). MC3E provided an opportunity to develop new retrieval
133 methods to estimate cloud microphysics and precipitation properties in precipitation systems



134 (Giangrande et al., 2014; Williams, 2016; Tian et al., 2016; Tian et al, 2018). Several stratiform
135 rain cases were observed by the VPRs during MC3E (as shown in Fig. 1). Distinct signatures of
136 “bright banding” are detected from VPRs. To retrieve LWP associated with stratiform
137 precipitation, this study mainly uses the observations from two co-located VPRs operating at 3-
138 GHz and 35-GHz at DOE ARM SGP Climate Research Facility.

139 **2.1 Vertical Pointing Radars**

140 The 3-GHz (S-band) VPR was deployed by NOAA Earth System Research Laboratory
141 for the six-weeks during the MC3E. The NOAA 3-GHz VPR is a vertical pointing radar with
142 2.6° beamwidth monitoring precipitation overhead. This 3-GHz profiler bridges the gap between
143 cloud radars, which are used to provide the structure of nonprecipitating clouds but are severely
144 attenuated by rainfall, and precipitation radars, which, although unattenuated by rainfall,
145 generally lack the sensitivity to detect more detailed cloud structure. The 3-GHz VPR observes
146 the raindrops within the Rayleigh scattering regime and its signal attenuation are negligible
147 through the rain. The temporal resolution of the profiles of Doppler velocity spectra is 7 seconds
148 and the vertical resolution is 60 meters. The 3-GHz VPR operated in two modes: a precipitation
149 mode and a low-sensitivity mode. The precipitation mode observations are used in this study.

150 The Ka-band ARM zenith radar (KAZR) is also a vertical pointing radar, operating at 35
151 GHz permanently deployed by DOE ARM at the SGP site. The KAZR measurements include
152 reflectivity, vertical velocity, and spectral width from near-ground to 20 km. The KAZR data
153 used in this study are the KAZR Active Remote Sensing of Clouds (ARSCL) product produced
154 by the ARM (www.arm.gov). The KAZR-ARSCL corrects for atmospheric gases attenuation
155 and velocity aliasing. By selecting the mode with the highest signal-to-noise ratio at a given
156 point, data from two simultaneous operating modes (general and cirrus mode) are combined for



157 each profile to provide the “best estimates” of radar moments in the time-height fields. The
158 vertical and temporal resolutions of KAZR-ARSCL product are 30 meters and 4 seconds,
159 respectively. Since the 3-GHz and 35-GHz VPRs are independent radars with different dwell
160 time and sample volumes (Williams et al., 2016), the radar observations are processed to 1-min
161 temporal and 60-m vertical resolutions in this study.

162 **2.2 Disdrometers**

163 DOE ARM program maintains a suite of surface precipitation disdrometers.
164 Measurements and estimations from the Distromet model RD-80 disdrometer and NASA two-
165 dimensional video disdrometers (2DVD) deployed at the ARM SGP site are used in this study.
166 The RD-80 disdrometer provides the most continuous raindrop size distribution (DSD)
167 measurements at high spectral (20 size bins from 0.3 to 5.4 mm) and temporal resolutions (1
168 minute), and its minimal detectable precipitation amount is 0.006 mm hr⁻¹. From 2DVD, the rain
169 DSDs are observed from 41 bins (0.1 - 10 mm), and its minimal detectable precipitation amount
170 is 0.01 mm hr⁻¹. In addition to rain rate, the mean mass-weighted raindrop diameter (D_m) is also
171 provided from 2DVD, which is used for evaluating retrieved D_m from radar measurements.

172 **2.3 Ceilometer**

173 A Vaisala laser ceilometer (CEIL) operates at the SGP Central Facility, sensing cloud
174 presence up to a height of 7700m with 10-m vertical resolution. The laser ceilometer transmits
175 near-infrared pulses of light, and the receiver detects the light scattered back by clouds and
176 precipitation. It is designed to measure cloud-base height.

177

178 **3. The Methodology of Liquid Water Path Estimation**

179 As mentioned earlier, both RLWP and CLWP contribute to the LWP. With aid of the
180 cloud base height detected by ceilometer, LWP is retrieved under two different situations: (I) the



181 cloud base is higher than the melting base and (II) the cloud base is lower than the melting base.
182 For situation (I), there are almost no cloud droplets below melting base ($CLWP = 0$), and thus
183 the LWP below the melting base is solely from raindrops. The LWP is calculated by integrating
184 RLWCs over this layer. The RLWCs could be retrieved by analyzing the measured Doppler
185 Velocity Differences (“*DVD Algorithm*”) from two collocated VPRs. In situation (II), the small
186 cloud droplets and large raindrops coexist below the melting base. Both raindrops and cloud
187 particles contribute to LWP. RLWP will be still estimated using “*DVD Algorithm*”. CLWP will
188 be retrieved using an attenuation-based algorithm named as “*Attenuation Algorithm*”. The
189 algorithms for LWP estimation are summarized in a flowchart (Fig. 2).

190 **3.1 Situation I (no cloud droplets exist below the melting base)**

191 The algorithm from Williams et al. (2016) was developed based on an assumption that
192 the 3-GHz VPR operates within the Rayleigh scattering regime for all raindrops, while the 35-
193 GHz VPR operates within the Rayleigh scattering regime for small raindrops (diameters $< \sim 1.3$
194 mm) and non-Rayleigh scattering regime for larger raindrops (diameters $\geq \sim 1.3$ mm). The
195 different scattering regimes for the two operating frequencies result in different estimated radar
196 moments. These estimated radar moments are in functions of rain microphysics. Thus, the rain
197 microphysics could be retrieved with given measured radar moments. The details of this “*DVD*
198 *Algorithm*” and uncertainty estimation are introduced in Appendix A.

199 **3.2 Situation II (cloud particles and rain droplets coexist below the melting base)**

200 In situation (II), substantial cloud particles exist below melting base, and both RLWP and
201 CLWP retrievals are needed to estimate the LWP. The total two-way attenuation of 35-GHz
202 VPR signals, A (in decibels, dB), in a layer between the melting base and the cloud base, mainly



203 consists of rain attenuation, liquid clouds attenuation, and gaseous attenuation. The total
 204 attenuation (A) are expressed as:

$$205 \quad A = 2 C R_m \Delta H + 2 B \text{ CLWP} + G. \quad (1)$$

206 R_m is layer-mean rain rate, and ΔH (km) is the thickness of the layer (Matrosov, 2009). G is the
 207 two-way attenuation/absorption from atmospheric gases, which is relatively small, and the
 208 absorption by gases has been already corrected in the KAZR ARSCL dataset and is assumed to
 209 be zero in our retrieval.

210 C and B are the coefficients for rainfall and cloud liquid water attenuation.

$$211 \quad B = 0.0026\pi\lambda^{-1} \text{Im}[-(m^2-1)(m^2+2)^{-1}], \quad (2)$$

212 where λ is the wavelength of Ka-band radar, and m is the complex refractive index of water.

213 The unit of B is dB/g m².

$$214 \quad C = 0.27 b, \quad (3)$$

215 where b is the correction factor considering raindrop fall velocities with changing air density.

$$216 \quad b = (\rho_{\text{am}}/\rho_{\text{a0}})^{0.45}, \quad (4)$$

217 where ρ_{am} and ρ_{a0} are the mean air density in the rain layer and the density at normal atmospheric
 218 conditions.

219 Based on (1), CLWP can be written as:

$$220 \quad \text{CLWP} = \frac{A - 2 C R_m \Delta H - G}{2 B} \quad (5)$$

221 The attenuation (A) is estimated by comparing the drop in Ka-band reflectivity with the
 222 un-attenuated S-band reflectivity through the cloud. Assuming the changes in reflectivity with
 223 altitude due to changes in raindrop size distributions with altitude are similar for Ka- and S-band
 224 reflectivities, then the difference in reflectivities through the cloud is a proxy for attenuation.

225 This can be expressed using



226
$$A \cong [Z_{Ka}(\text{cloud base}) - Z_{Ka}(\text{melting base})] - [Z_S(\text{cloud base}) - Z_S(\text{melting base})] \quad (6)$$

227 Notice that the absolute calibration of the radar was not important to the retrieval results since
228 the retrieval of CLWP used S-Ka differential attenuation. This avoids the radar calibration
229 (Tridon et al., 2015 and 2017), which is a serious issue limits the accuracy of radar retrievals.

230 The R_m is estimated as:

231
$$R_m = \frac{\sum_{CB}^{MB} RR(h) \times \Delta h}{\Delta H}, \quad (7)$$

232 where Δh equals 60 meters and MB and CB are the melting base and the cloud base. RRs in the
233 layer between the melting base and the cloud base are calculated from the “*DVD algorithm*”.

234 The uncertainties of retrieved CLWP are mainly due to the uncertainties of estimated R_m
235 and observed total attenuation from VPRs. The value of B_k is on the order of 1 dB/kg m⁻². The
236 uncertainty of retrieved CLWP would be ~ 0.25 kg m⁻² with 0.5 dB uncertainty from measured
237 radar reflectivity difference or ~ 0.5 kg m⁻² for 1.0 mm hr⁻¹ uncertainty from estimated layer-
238 mean rain rate. Compared to the typical mean rain rate observed in the stratiform system ($\sim 2 - 4$
239 mm hr⁻¹), 1.0 mm hr⁻¹ represents a $\sim 30\%$ uncertainty. The uncertainty for CLWP retrievals is
240 roughly estimated as ~ 0.56 kg m⁻² (sqrt (0.25²+0.5²)) in this study. For reference, the expected
241 uncertainty is reported as ~ 0.25 kg m⁻² for typical rainfall rates ($\sim 3 - 4$ mm hr⁻¹) in Matrosov
242 (2009) retrieval method.

243

244 **4. Retrieval Results and Discussions**

245 **4.1 Case Studies**

246 Even though situation (I) is dominated (Fig. 1), especially in Case A, the ceilometer
247 cloud base estimates can be lower than the melting base (Cases B to D). Two case studies (20



248 May 2011 and 11 May 2011) are given as examples to demonstrate the estimation of LWP in
249 stratiform precipitation system for two different situations.

250 **4.1.1 Case A**

251 On 20 May 2011, an upper level low-pressure system at central Great Basin moved into
252 the central and northern Plains, while a surface low pressure at southeastern Colorado brought
253 the warm and moist air from the southern Plains to a warm front over Kansas. and a dry line
254 extended southward from the Texas-Oklahoma. With those favorable conditions, a strong north-
255 south oriented squall line developed over Great Plains and propagated eastward. The convection
256 along the leading edge of this intense squall line exited the ARM SGP network around 11 UTC
257 20 May leaving behind a large area of stratiform rain (Case A in Fig. 1). This stratiform system
258 passed over the ARM SGP site and observed by two VPRs, and disdrometers as shown in
259 Figures 1a-1c. It clearly shows the 3-GHz radar echo tops are much lower than those from the
260 35 GHz VPR. Even though there is attenuation at 35-GHz by the raindrops and melting
261 hydrometeors, the 35-GHz radar can still detect more small ice particles at near the cloud top.
262 The “bright band”, which occurs in a uniform stratiform rain region, is clearly seen from the 3-
263 GHz VPR (a sudden increase and then decrease in radar reflectivity) but is not obvious from the
264 35-GHz VPR due to the non-Rayleigh scattering effects at 35 GHz (Sassen et al., 2005;
265 Matrosov, 2008).

266 Figures 1a-1b clearly show that the ceilometer detected cloud base is in the middle of the
267 melting layer, indicating almost no cloud particles below the melting layer and the LWP in the
268 liquid layer equals to RLWP. The RLWP is retrieved using the “*DVD Algorithm*” introduced in
269 section 3.1 and Appendix A. Figure 3 shows an example of the DVD retrieval algorithm at
270 13:40 UTC on May 20, 2011. Radar reflectivity from 3 GHz, Doppler velocities from 3 GHz



271 and 35 GHz, and spectrum variance from 35 GHz are the inputs of DVD algorithm. The
272 Doppler velocity differences (3 GHz – 35 GHz) from the surface to 4 km are also plotted in Fig.
273 3d. The melting base is defined as the height of maximum curvature in the radar reflectivity
274 profile at 3 GHz (Fabry and Zawadzki, 1995), which is clearly seen at 2.5 km in Fig. 3. Below
275 2.5 km, the Doppler velocity differences between the two VPRs become relatively uniform,
276 indicating that the process of melting snow/ice particles into raindrops is completed. Retrieved
277 profiles of rain microphysical properties and their corresponding uncertainties (horizontal bars at
278 different levels) in the rain layer (0 – 2.5 km) are shown in Figs 3f-3h. In general, the retrieved
279 D_m values from the surface to 2.5 km are nearly a constant of ~ 2 mm (Fig. 3f), while the
280 retrieved RLWC and rain rate values slightly decrease from 2.5 km to the surface. One of the
281 highlights of this study is, in addition to the surface rain rate, which can usually be observed
282 using surface disdrometers, the vertical profiles of rain microphysical properties are retrieved.
283 These retrieved rain microphysical properties will shed light on the understanding of liquid cloud
284 and rain microphysical processes (like condensation, evaporation, autoconversion and accretion
285 etc.) in the models.

286 To evaluate the rain property retrievals, we compare the retrieved rain microphysical
287 properties, the D_m , and rain rate at the surface, with the surface disdrometers measurements (Fig.
288 4). The D_m values range from 1.0 to 2.5 mm during a 3.5-hr period with nearly identical mean
289 values of 1.79 mm and 1.81 mm from both retrievals and 2DVD measurements. There are large
290 variations for rain rates, ranging from 0 to 8 mm hr⁻¹, with means of 3.19, 3.17 and 2.88 mm hr⁻¹,
291 respectively, from 2DVD, RD-80 and radar retrieval. The mean rain rates from 2DVD and RD-
292 80 measurements are almost the same although there are relatedly large differences during
293 certain time periods, while the retrievals from this study, on average, underestimate the rain rate



294 by ~10% compared to the disdrometer measurements. More statistics (mean differences, their 95%
295 confidence intervals of mean differences and root mean square errors) can be found in Table 2.
296 Overall, the mean differences are within the retrieval uncertainties. The variation of RLWP (Fig.
297 4c) mimics the variation of retrieved rain rate in Fig. 4d. The mean value of RLWP is 0.56 kg m⁻²
298 for this case, which is also the LWP below the melting base.

299 **4.1.2 Case B**

300 On 11 May 2011, a surface cold front moved across the Oklahoma-Texas area and then
301 convections were initiated. At 1600 UTC, a mesoscale convective system organized with a
302 parallel stratiform precipitation region. Two-three hours later (~1830 UTC), the mesoscale
303 convective system was transitioned to a trailing stratiform mode passed over the ARM SGP site.
304 The large stratiform regions are observed by two VPRs and disdrometers as shown in Figs 1d-1f.
305 Figures 1d-1f clearly show that the ceilometer detected cloud bases are lower than the melting
306 bases occasionally. Under this situation, both RLWP and CLWP could contribute to the LWP
307 below the melting base.

308 Firstly, the surface rain microphysics (D_m , RLWC, rain rate and RLWP) are retrieved
309 using “*DVD Algorithm*”. These rain property retrievals are compared with the surface
310 disdrometers measurements (Fig. 5). The D_m values at the surface range from 0.8 to 2.2 mm
311 during a 4.5-hr period with the mean values of 1.46 mm and 1.57 mm, respectively, from both
312 retrievals and 2DVD measurements. The difference between the retrieval and 2DVD
313 measurement may be due to different sampling volumes between radar and the surface
314 disdrometer, as well as wind shear. To further investigate the difference, the measurements from
315 five NASA 2DVDs located within 5 km away from VPRs are collected and processed. The
316 almost same mean values and slight variation from 5 NASA 2DVDs measurements suggest that



317 the difference between radar retrievals and the surface disdrometer measurements may be true,
318 while averaging from more measurements can only smooth the variation.

319 The mean rain rate values from five NASA 2DVDs and the surface disdrometer are very
320 comparable, with a mean difference of 0.3 mm hr^{-1} . The almost same mean values between the
321 surface disdrometer and 5 NASA 2DVDs measurements suggest that the DVDs apart within 5
322 km can capture very similar rain properties during a longer time period, such as 4.5 hours in this
323 case, although there are some large differences from their point-to-point measurements. The rain
324 rates, in this case, vary quite large, ranging from 0 to 9 mm hr^{-1} with means of 1.81, 1.64 and
325 1.98 mm hr^{-1} , respectively from single 2DVD, RD-80, and our retrieval. It is found that, from
326 both Case A and Case B, the mean value from RD-80 is smaller than that from 2DVD. This may
327 be due to the different ranges of measurable drop sizes from two types of disdrometers ($0.3 - 5.4$
328 mm for RD 80, while 0.1 to 10 mm for 2DVD). More statistics can be also found in Table 2.
329 Overall, the mean differences are still within the retrieval uncertainties for this case.

330 Secondly, the CLWP is retrieved using “Attenuation Algorithm” introduced in section
331 3.2. Figure 5c shows the time series of RLWP, CLWP and LWP retrievals. It is found that the
332 CLWP values (when they exist) are usually larger than RLWP values in the same vertical
333 column. When cloud droplets and raindrops coexist below the melting base, the mean values are
334 0.31 kg m^{-2} and 1.00 kg m^{-2} for RLWP and CLWP, and the corresponding LWP below the
335 melting layer is 1.31 kg m^{-2} . While when only raindrops exist below the melting base, there is no
336 CLWP (CLWP =0), and the RLWP and LWP are the same (with average of 0.33 kg m^{-2}). It is
337 noticed that even though the occurrence of CLWP is low (12%) in this case, the value of CLWP
338 can be very large when it exists, and it is about two times larger than the mean RLWP. The
339 mean value of LWP is 0.45 kg m^{-2} for all the sample in Fig. 5c.



340 4.2 Statistical Results

341 Box and whisker plots of retrieved RLWP, CLWP and LWP for situations (I), (II) and all
342 samples during MC3E are shown in Fig. 6. The horizontal orange and red dashed lines indicate
343 the median and mean, boundaries of the box represent the first and third quartiles, and the
344 whiskers are the 10th- and 90th -percentiles. During MC3E, a total of 14 hours of stratiform rain
345 were observed by VPRs at the ARM SGP Climate Research Facility, in which 92% and 8% the
346 samples are categorized into the situations (I) and (II), respectively. The mean RLWPs are 0.33
347 kg m⁻² and 0.22 kg m⁻² for the situations (I) and (II). There are a substantial amount of small
348 cloud droplets sustaining in the rain layer and have not yet converted to larger raindrops, which
349 may partially explain smaller RLWP in the situation (II). The mean value of surface rain rate is
350 1.78 mm hr⁻¹ when cloud droplets exist, which is also smaller than the mean value (2.06 mm hr⁻¹)
351 in the rain-only situation. The mean CLWP in the situation (II) is as large as ~0.87 kg m⁻² even
352 though their occurrence is very low (8%), which is much larger than mean RLWP in the liquid
353 layer. The ratio of RLWP and CLWP ranges from 4:1 to 2:1 for precipitating shallow marine
354 clouds reported at Lebsock et al. (2011), while our results from MC3E do not seem to have a
355 clear linear relationship between CLWP and RLWP (figure is not shown). The LWP from the
356 situation (II) is much larger than the mean LWP from the situation (I), which is primarily
357 contributed by cloud droplets. The overall mean LWP for stratiform rain during MC3E is 0.39
358 kg m⁻².

359 We also processed the ARM MWR retrieved LWPs during MC3E and compared with
360 our retrievals as illustrated in Fig. 7. Statistical results of the retrieved LWPs from this study and
361 MWR are averaged for each measured rain rate bins (bin size = 0.25 mm hr⁻¹). When the rain
362 rate is greater than ~ 6mm hr⁻¹, there are no MWR LWP retrievals. Fig. 7b shows that the MWR
363 retrieved LWPs, as expected, monotonically increase with rain rate, which is possible due to the



364 “wet radome” effect (Cadeddu et al., 2017). “Wet radome” is a particularly complicated
365 situation because the standing water often looks physically like a layer and less like a collection
366 of drops, making the MWR overestimate LWPs (personal communication with Dave Turner,
367 2018), and so far, no effective method was found to solve this problem (Cadeddu et al., 2017).

368 In addition to the issue from standing water on the radome, the scattering effects due to
369 raindrops also affect MWR retrievals. Two general retrieval methods are commonly used to
370 retrieve LWP from the observed brightness temperatures: statistical methods (Liljegren et al.,
371 2001) and physical retrievals (Turner et al, 2007). No matter which retrieval is used, the
372 radiative transfer code usually only models the absorptions from atmospheric gases and cloud
373 liquid water. The scattering effect is not taken into consideration during the retrieval, that is, it is
374 under the assumption that the brightness temperature is primarily due to the emission of cloud
375 droplets in the MWR retrieval. Even small drizzle particles still have a scattering effect, which
376 could contribute higher brightness temperature measured by MWR and result in larger retrieved
377 LWPs than the “true” LWPs. Therefore, the MWR retrieved LWPs are most likely
378 overestimated for precipitating clouds.

379 In this study, we mainly focus on the stratiform rain systems with mean rain rates of 2-4
380 mm hr⁻¹. The scattering effect for large raindrops is more significant than drizzles. Sheppard
381 (1996) examined the effect of raindrops on MWR brightness temperature measurements at 31
382 GHz and found that cloud absorption coefficient is only ~2/3 of rain absorption coefficient,
383 however, the scattering effect of raindrops is not insignificant where its scattering coefficient is
384 about half of cloud absorption coefficient. Thus, MWR measured brightness temperatures for
385 precipitating clouds would be higher, due to the scattering by raindrops, than those for non-
386 precipitating clouds, and then result in higher LWPs than the ‘true’ LWPs. The differences of



387 LWPs from MWR and this study are shown in Fig. 7c. The LWP differences increase almost
388 linearly with increased rain rate. The differences could be due to (1) MWR retrieved LWP
389 represents the whole vertical column (RWLP and CLWP below melting layer, large water coated
390 ice particles in the melting layer and supercooled LWCs above the melting layer), while our
391 retrieval only represent the LWP below the melting base; (2) existing uncertainty in retrieved
392 LWP from this study ($\sim 0.6 \text{ kg m}^{-2}$ when including CLWP estimates).

393

394 **5. Summary and Conclusions**

395 LWP is a critical parameter for studying clouds, precipitation, and their life cycles. LWP
396 can be retrieved from microwave radiometer measured brightness temperatures during cloudy
397 and light precipitation conditions. However, MWR-retrieved LWPs are questionable under
398 moderate and heavy precipitation conditions due to the “wet radome” and non-Rayleigh
399 scattering effects caused by large raindrops. LWPs below the melting base in stratiform
400 precipitation systems are estimated, which include both RLWP and CLWP. The measurements
401 used in this study are mainly from two VPRs, 35-GHz from ARM and 3-GHz from NOAA
402 during the MC3E field campaign.

403 In this study, the microphysical properties of raindrops, such as D_m , RLWC (and RLWP),
404 and RR, are estimated following the method described in Williams et al. (2016) using
405 measurements from co-located Ka- and S-band radars VPRs. The retrieved rain microphysical
406 properties are validated by the surface disdrometer measurements. Instead of retrieving vertical
407 air motion and rain DSDs (Williams et al., 2016), this study aims at retrieving RLWCs and then
408 integrating RLWCs over the liquid layer to estimate RLWP. The CLWP is retrieved based on



409 the modifications of the methods in Matrosov (2009 and 2010) with available radar
410 measurements, vertical pointing Ka- and S-band VPRs, during the MC3E field campaign.

411 The applicability of retrieval methods is illustrated for two stratiform precipitation cases
412 (20 May 2011 and 11 May 2011) observed during MC3E. Statistical results from a total of 14
413 hours samples during MC3E show that the occurrence of cloud droplets below the melting base
414 is low (8%), while the CLWP value can be up to 0.87 kg m^{-2} , which is much larger than the
415 RLWP (0.22 kg m^{-2}). When only raindrops exist below the melting base, the averaged RLWP
416 value is 0.33 kg m^{-2} , which is much larger than the mean RLWP in the cloud droplets and
417 raindrops coexisted situation.

418 Reliable retrievals of RLWC and RLWP are critical for model evaluation and
419 improvement, as RLWC (rain mixing ratio) is an important prognostic variable in weather and
420 climate models. Furthermore, the retrievals in the whole rain layer would be useful to
421 understand the microphysical processes (i.e., condensation, evaporation, autoconversion, and
422 accretion etc.) and have great potential to improve model parametrizations in the future. Overall,
423 the LWP (CLWP and RLWP) retrievals derived in this study can be used to evaluate the models
424 that separately predict cloud and precipitation separately, and contribute comprehensive
425 information to study cloud-to-precipitation transitions.

426

427 **Appendix A: Doppler Velocity Differences Algorithm (“DVD Algorithm”)**

428 Retrieving RLWC and other rain microphysical properties (i.e., drop size and rain rate) is
429 based on the mathematics of DSD radar reflectivity-weighted velocity spectral density S_{DSD}^{λ}
430 [$(\text{mm}^6 \text{ m}^{-3}) (\text{m s}^{-1})^{-1}$], which is a product of radar raindrop backscattering cross section $\sigma_b^{\lambda}(D)$
431 (mm^2) and DSD number concentration $N_{DSD}(D)$ ($\text{mm}^{-1} \text{ m}^{-3}$):



432
$$S_{\text{DSD}}^{\lambda}(v_z) = \left[\frac{\lambda^4}{\pi^5 |K_w|^2} \sigma_b^{\lambda} \right] N_{\text{DSD}}(D) \frac{dD}{dv_z}. \quad (\text{A1})$$

433 The $\frac{dD}{dv_z}$ [mm (m s⁻¹)⁻¹] is used as a coordinate transformation from diameter to velocity,
 434 where v_z (m s⁻¹) is the raindrop terminal velocity of diameter D (mm) at altitude z . λ is the
 435 wavelength of radar. $|K_w|^2$ equals 0.93 and it is the dielectric factor.

436 The $N_{\text{DSD}}(D)$ can be expressed as a normalized gamma shape distribution with a three
 437 parameters (Leinonen et al., 2012):

438
$$N_{\text{DSD}}(D; N_w, D_m, \mu) = N_w f(D; D_m, \mu), \quad (\text{A2})$$

439 where

440
$$f(D; D_m, \mu) = \frac{6}{4^4} \frac{(\mu+4)^{(\mu+4)}}{\Gamma(\mu+4)} \left(\frac{D}{D_m}\right)^{\mu} \exp\left[-(\mu+4) \frac{D}{D_m}\right]. \quad (\text{A3})$$

441 N_w is the scaling parameter, μ is a shape parameter, $\Gamma(x)$ is the Euler gamma function, and D_m is
 442 a mean mass-weighted raindrop diameter estimated from the ratio of the fourth to third DSD
 443 moments:

444
$$D_m = \frac{M_4}{M_3} = \frac{\int_{D_{\min}}^{D_{\max}} N_{\text{DSD}}(D) D^4 dD}{\int_{D_{\min}}^{D_{\max}} N_{\text{DSD}}(D) D^3 dD}. \quad (\text{A4})$$

445 where D_{\min} and D_{\max} represent the minimum and maximum diameters in the distribution,
 446 respectively.

447 The intrinsic (non-attenuation) reflectivity factor and the mean velocity and the spectrum
 448 variance are the zeroth, first, and second reflectivity-weighted velocity spectrum moments :

449
$$Z_{\text{DSD}}^{\lambda} = \sum_{v_{\min}}^{v_{\max}} S_{\text{DSD}}^{\lambda}(v_i) \Delta v \quad (\text{A5})$$

450
$$v_{\text{DSD}}^{\lambda} = \frac{\sum_{v_{\min}}^{v_{\max}} S_{\text{DSD}}^{\lambda}(v_i) v_i \Delta v}{Z_{\text{DSD}}^{\lambda}} \quad (\text{A6})$$

451
$$SV_{\text{DSD}}^{\lambda} = \frac{\sum_{v_{\min}}^{v_{\max}} (v_i - v_{\text{DSD}}^{\lambda})^2 S_{\text{DSD}}^{\lambda}(v_i) \Delta v}{Z_{\text{DSD}}^{\lambda}}. \quad (\text{A7})$$



452 where v_i is the discrete velocities and Δv is velocity resolution in the integration.

453 The Doppler Velocity Difference (DVD) is defined as

$$454 \quad \text{DVD} = v_{\text{DSD}}^{3 \text{ GHz}} - v_{\text{DSD}}^{35 \text{ GHz}}. \quad (\text{A8})$$

455 Note that both DVD and SV are dependent on DSD parameters (D_m and μ) only.

456 The RLWC and rain rate (RR) can also be described using the DSD:

$$457 \quad \text{RLWC}(\text{g m}^{-3}) = \frac{\pi}{6} 10^{-3} \sum_{D_{\text{min}}}^{D_{\text{max}}} N_{\text{DSD}}(D, N_w, D_m, \mu) D_i^3 \Delta D \quad (\text{A9})$$

$$458 \quad \text{RR}(\text{mm hr}^{-1}) = \frac{6\pi}{10^4} \sum_{D_{\text{min}}}^{D_{\text{max}}} N_{\text{DSD}}(D, N_w, D_m, \mu) D_i^3 v_z(D_i) \Delta D. \quad (\text{A10})$$

459 In addition, there are two newly defined radar-related parameters ($Z_{3\text{GHz}}\text{LWC}$ and $Z_{3\text{GHz}}\text{RR}$),

460 which are also dependent on D_m and μ only:

$$461 \quad Z_{3\text{GHz}}\text{LWC} = 10 \log_{10}(Z_{\text{DSD}}^{3\text{GHz}}/\text{RLWC}) \quad (\text{A11})$$

$$462 \quad Z_{3\text{GHz}}\text{RR} = 10 \log_{10}(Z_{\text{DSD}}^{3\text{GHz}}/\text{RR}) \quad (\text{A12})$$

463 In this study, four variables, DVD, SV at 35 GHz ($\text{SV}_{35\text{GHz}}$), $Z_{3\text{GHz}}\text{LWC}$ and $Z_{3\text{GHz}}\text{RR}$, are
 464 pre-calculated using different groups of D_m and μ values, and then these values are stored in
 465 look-up tables (LUTs). Raindrop backscattering cross sections are calculated using the T-matrix
 466 with different temperatures and oblate raindrop axis ratios (Leinonen, 2014). LUT examples are
 467 illustrated in Fig. A as functions of DVD and $\text{SV}_{35\text{GHz}}$. If we assume that the observed radar
 468 Doppler velocity difference and spectrum variance from the 35-GHz radar is equal to the DSD
 469 velocity difference and variance (DVD and $\text{SV}_{35\text{GHz}}$), the measured Doppler velocity difference
 470 and spectrum variance at 35-GHz can determine a solution for D_m from the LUT (Fig. A(a)).
 471 Similarly, a value of $Z_{3\text{GHz}}\text{LWC}$ (or $Z_{3\text{GHz}}\text{RR}$) can be found with measured DVD and $\text{SV}_{35\text{GHz}}$
 472 using the LUT in Fig. A(b) (or Fig. A(c)). Then RLWC (or RR) can be estimated using (A11)
 473 (or (A12)) with measured reflectivity at 3-GHz ($Z_{3\text{GHz}}$).



474 The observed radar Doppler velocity difference can be assumed to be equal to the DSD
475 velocity difference for two reasons: (1) even though the radar observed Doppler velocity
476 spectrum can be broadened by the air motion, this spectrum broadening variance is small (within
477 2%) relative to the DSD velocity spectrum because of the narrow beamwidth (0.2°) of KAZR
478 and (2) spectrum broadening is symmetric, which does not affect the first spectrum moment and
479 the DSD mean Doppler velocity only shifts due to the air motion. Therefore, the measured
480 differences of Doppler velocity between the 3-GHz and 35- GHz radars vertical pointing
481 observations are independent of air motion and can be assumed to be the same as DVD from
482 (A8). The validity of such an assumption is fully discussed in Williams et al. (2016).

483 The variabilities of 3-GHz and 35-GHz VPR observations within each 1-minute/60-meter
484 bin are regarded as the measurement uncertainties and will be propagated through the retrieval to
485 produce retrieval uncertainties. The retrieval uncertainties are estimated follow two steps: (1)
486 construct a distribution of input radar measurements. For example, the temporal resolution for 3-
487 GHz VPR is seven seconds, thus there are about nine radar reflectivities observed for one minute.
488 A normal distribution is generated first using the mean and standard deviations of these nine
489 observed radar reflectivities for this 1-min/60-m resolution/bin. (2) repeat the DVD retrievals
490 using samplings from distributions of all input measurements. We randomly select 100 groups
491 of members from those (DVD, $SV_{35\text{GHz}}$, $Z_{3\text{GHz}}$) normal distributions to form 100 realizations, and
492 then produce 100 separate output estimates. The mean and standard deviation of the 100
493 solutions are regarded as the final retrieval and the retrieval uncertainty.

494 It is noted that the uncertainty here only considers estimates of instrument noise, not the
495 uncertainties associated with assumptions used in the retrieval. For example, the gamma size
496 distribution used in (A2) is an approximation which may introduce error into the retrieval.



497 However, it is very difficult to quantify this type of retrieval uncertainty. In this study, we
498 further compared our retrievals with independent surface disdrometers measurements to estimate
499 the uncertainties of retrievals. Also, when both radars are observing at Rayleigh scattering for
500 small raindrops, the reflectivity-weighted radial velocities for these particles should be the same.
501 In order to have a difference in radial velocity during the retrieval, large droplets must exist. The
502 maximum diameters in drop size distribution measured from disdrometer for all the stratiform
503 cases during MC3E are investigated. It is found that the occurrence of small-droplets-only
504 (maximum diameter <1.3 mm) is very low (less than 3%). Thus, it will not have a significant
505 impact on the retrieval results. Notice that this algorithm is not suitable for strong convective
506 rain due to the wind shear and strong turbulence as well as severe attenuation and extinction of
507 the Ka-band radar signal.

508

509 **Acknowledgments:** J. Tian and X. Dong are supported by DOE CMDV project under grant DE-
510 SC0017015 at the University of Arizona, and B. Xi is supported by NASA CERES project under
511 grant NNX17AC52G at the University of Arizona. C. R. Williams is supported by DOE ASR
512 project under grant DE-SC0014294. Special thanks to Dr. Sergey Matrosov from NOAA Earth
513 System Research Laboratory (ESRL) for his suggestions. Special thanks to Michael Jensen, PI
514 of MC3E. Aircraft in situ measurements are processed using data from
515 <https://ghrc.nsstc.nasa.gov/pub/fieldCampaigns/gpmValidation/mc3e/>, can also be obtained from
516 Xiquan Dong (xdong@email.arizona.edu). NOAA vertical profile radar datasets are publically
517 available in the DOE archives ([http://iop.archive.arm.gov/arm-iop/2011/sgp/mc3e/williams-](http://iop.archive.arm.gov/arm-iop/2011/sgp/mc3e/williams-s_band/)
518 [s_band/](http://iop.archive.arm.gov/arm-iop/2011/sgp/mc3e/williams-s_band/)).

519



520 **References**

- 521 Ackerman, T. P., and Stokes, G. M: The Atmospheric Radiation Measurement Program. *Phys.*
522 *Today*, 56,38–44, doi:10.1063/1.1554135, 2003
- 523 Battaglia, A., Saavedra, P., T. Rose, and Simmer, C.: Characterization of precipitating clouds by
524 ground-based measurements with the triple-frequency polarized microwave radiometer
525 ADMIRARI, *J. Appl. Meteorol.*, 49(3), 394–414, 2009
- 526 Cadeddu, M. P., Liljegren, J. C., and Turner, D. D.: The Atmospheric radiation measurement
527 (ARM) program network of microwave radiometers: instrumentation, data, and retrievals,
528 *Atmos. Meas. Tech.*, 6, 2359-2372, <https://doi.org/10.5194/amt-6-2359-2013>, 2013
- 529 Cadeddu, M. P., Marchand, R., Orlandi, E., Turner, D. D. and Mech, M. (2017). Microwave
530 Passive Ground-Based Retrievals of Cloud and Rain Liquid Water Path in Drizzling
531 Clouds: Challenges and Possibilities, *IEEE Transactions on Geoscience and Remote*
532 *Sensing*, vol. 55, no. 11, pp. 6468-6481, doi: 10.1109/TGRS.2017.2728699
- 533 Crewell, S., and Löhnert, U. (2003). Accuracy of cloud liquid water path from ground-based
534 microwave radiometry 2. Sensor accuracy and synergy, *Radio Sci.*, 38, 8042,
535 doi:10.1029/2002RS002634, 3.
- 536 Dubrovina, L. S.: Cloudness and precipitation according to the data of airplane soundings,
537 *Gidrometeoizdat, Leningrad* (in Russian), 218 pp,1982
- 538 Ellis, S. M., and Vivekanandan, J.: Liquid water content estimates using simultaneous S and K_a
539 band radar measurements, *Radio Sci.*, 46, RS2021, doi:10.1029/2010RS004361, 2011
- 540 Fabry, F. and Zawadzki, I.: Long-Term Radar Observations of the Melting Layer of Precipitation
541 and Their Interpretation. *J. Atmos. Sci.*, 52, 838–851, [https://doi.org/10.1175/1520-](https://doi.org/10.1175/1520-0469(1995)052<0838:LTROOT>2.0.CO;2)
542 [0469\(1995\)052<0838:LTROOT>2.0.CO;2](https://doi.org/10.1175/1520-0469(1995)052<0838:LTROOT>2.0.CO;2), 1995



- 543 Fan, J., Liu, Y.-C., Xu, K.-M., North, K., Collis, S., Dong, X., and Ghan, S. J.: Improving
544 representation of convective transport for scale-aware parameterization:1. Convection
545 and cloud properties simulated with spectral bin and bulk microphysics, *Journal of*
546 *Geophysical Research: Atmosphere*, 120, 3485–3509,
547 <https://doi.org/10.1002/2014JD022142>, 2015
- 548 Feng, Z., Dong, X. Q., Xi, B. K., Schumacher, C., Minnis, P., and Khaiyer, M.: Top-of-
549 atmosphere radiation budget of convective core/stratiform rain and anvil clouds from
550 deep convective systems. *Journal of Geophysical Research*, 116, D23202. [https://doi.org/](https://doi.org/10.1029/2011JD016451)
551 [10.1029/2011JD016451](https://doi.org/10.1029/2011JD016451), 2011
- 552 Feng, Z., Leung, L. R., Houze, R. A., Jr., Hagos, S., Hardin, J., Yang, Q., Han, B. and Fan, J.:
553 Structure and evolution of mesoscale convective systems: Sensitivity to cloud
554 microphysics in convection-permitting simulations over the United States. *Journal of*
555 *Advances in Modeling Earth Systems*, 10, 1470–1494.
556 <https://doi.org/10.1029/2018MS001305>, 2018
- 557 Giangrande, S. E., Collis, S., Theisen, A. K., and Tokay, A.: Precipitation estimation from the
558 ARM distributed radar network during the MC3E campaign, *J. Appl. Meteorol. Climatol.*,
559 doi:10.1175/JAMC-D-13-0321.1, 2014
- 560 Jensen, M.P., Petersen, W. A., Bansemer, A., Bharadwaj, N., Carey, L. D., Cecil, D. J, and
561 Zipser, E. J.: The Midlatitude Continental Convective Clouds Experiment (MC3E),
562 *Bulletin of the American Meteorological Society*. 151221073208006.
563 <https://doi.org/10.1175/BAMS-D-14-00228.1>, 2015
- 564 Leinonen, J., Moisseev, D., M. Leskinen, M., and W.A. Petersen, W.A.: A Climatology of
565 Disdrometer Measurements of Rainfall in Finland over Five Years with Implications for



- 566 Global Radar Observations. *J. Appl. Meteor. Climatol.*, 51, 392–404,
567 <https://doi.org/10.1175/JAMC-D-11-056.1>, 2012
- 568 Leinonen, J.: High-level interface to T-matrix scattering calculations: architecture, capabilities
569 and limitations, *Opt. Express*, vol. 22, issue 2, 1655–1660 doi: [10.1364/OE.22.001655](https://doi.org/10.1364/OE.22.001655),
570 2014
- 571 Liljegren, J. C., Clothiaux, E. E., Mace, G. G., Kato, S., and Dong, X.: A new retrieval for cloud
572 liquid water path using a ground-based microwave radiometer and measurements of
573 cloud temperature, *J. Geophys. Res.*, 106(D13), 14485–14500,
574 doi:10.1029/2000JD900817, 2001
- 575 Lebsock, M.D., L’Ecuyer, T.S. and Stephens, G.L.: Detecting the Ratio of Rain and Cloud
576 Water in Low-Latitude Shallow Marine Clouds. *J. Appl. Meteor. Climatol.*, 50, 419–432,
577 <https://doi.org/10.1175/2010JAMC2494.1>, 2011
- 578 Matrosov, S. Y.: Assessment of radar signal attenuation caused by the melting hydrometeor layer.
579 *IEEE Trans. Geo Sci. Remote Sens.*, 46, 1039–1047 doi: [10.1109/TGRS.2008.915757](https://doi.org/10.1109/TGRS.2008.915757),
580 2008
- 581 Matrosov, S. Y.: A method to estimate vertically integrated amounts of cloud ice and liquid and
582 mean rain rate in stratiform precipitation from radar and auxiliary data, *J. Appl. Meteorol.*,
583 48, 1398–1410, doi:10.1175/2009JAMC2196.1, 2009
- 584 Matrosov, S. Y.: Synergetic use of millimeter- and centimeter-wavelength radars for retrievals of
585 cloud and rainfall parameters, *Atmos. Chem. Phys.*, 10, 3321–3331,
586 <https://doi.org/10.5194/acp-10-3321-2010>, 2010
- 587 Mazin, I. P. (Ed.): *Clouds and the Cloudy Atmosphere*. Gidrometeoizdat, Leningrad, 648 pp,
588 1989.



- 589 Saavedra, P., Battaglia, A., and Simmer, C.: Partitioning of cloud water and rainwater content by
590 ground-based observations with the Advanced Microwave Radiometer for Rain
591 Identification (ADMIRARI) in synergy with a micro rain radar, *J. Geophys. Res.*, 117,
592 D05203, doi:10.1029/2011JD016579, 2012
- 593 Sassen, K., Campbell, J. R., Zhu, J., Kollias, P., Shupe, M., and Williams, C.: Lidar and Triple-
594 Wavelength Doppler Radar Measurements of the Melting Layer: A Revised Model for
595 Dark- and Brightband Phenomena. *J. Appl. Meteor.*, 44, 301–312,
596 <https://doi.org/10.1175/JAM-2197.1>, 2005
- 597 Sheppard, B.E.: Effect of Rain on Ground-Based Microwave Radiometric Measurements in the
598 20–90-GHz Range. *J. Atmos. Oceanic Technol.*, 13, 1139–1151,
599 [https://doi.org/10.1175/1520-0426\(1996\)013<1139:EOROGB>2.0.CO;2](https://doi.org/10.1175/1520-0426(1996)013<1139:EOROGB>2.0.CO;2), 1996
- 600 Tian, J., Dong, X., Xi, B., Wang, J., Homeyer, C. R., McFarquhar, G. M., and Fan J.: Retrievals
601 of ice cloud microphysical properties of deep convective systems using radar
602 measurements, *Journal of Geophysical Research: Atmosphere.*, 121,10 ,820–10,839,
603 <https://doi.org/10.1002/2015JD024686>, 2016
- 604 Tian, J., Dong, X., Xi, B., Minnis, P., Smith, W. L., Jr, Sun-Mack, S., ... Wang, J.: Comparisons
605 of ice water path in deep convective systems among ground-based, GOES, and CERES-
606 MODIS retrievals. *Journal of Geophysical Research: Atmospheres*, 123, 1708–1723.
607 <https://doi.org/10.1002/2017JD027498>, 2018
- 608 Tridon, F., and Battaglia, A.: Dual-frequency radar Doppler spectral retrieval of rain drop size
609 distributions and entangled dynamics variables, *J. Geophys. Res. Atmos.*, 120, 5585–
610 5601, doi:10.1002/2014JD023023, 2015



- 611 Tridon, F., Battaglia, A., and Kollias, P.: Disentangling Mie and attenuation effects in rain using
612 a Ka-W dual-wavelength Doppler spectral ratio technique, *Geophys. Res. Lett.*, 40, 5548
613 5552, doi:10.1002/2013GL057454, 2013
- 614 Tridon, F., Battaglia, A., Luke, E., and Kollias, P.: Rain retrieval from dual-frequency radar
615 Doppler spectra: validation and potential for a 25 midlatitude precipitating case-study,
616 *Quarterly Journal of the Royal Meteorological Society*, 143, 1364–1380, 2017.
- 617 Turner, D. D., Clough, S. A., Liljegren, J. C., Clothiaux, E. E., Cady-Pereira, K. E., and Gaustad,
618 K. L.: Retrieving liquid water path and precipitable water vapor from the Atmospheric
619 Radiation Measurement (ARM) microwave radiometers. *IEEE Trans. Geosci. Remote*
620 *Sens.*, 45, 3680–3690, 2007
- 621 Wentz, F.J. and Spencer, R.W.: SSM/I Rain Retrievals within a Unified All-Weather Ocean
622 Algorithm. *J. Atmos. Sci.*, 55, 1613–1627, [https://doi.org/10.1175/1520-](https://doi.org/10.1175/1520-0469(1998)055<1613:SIRRWA>2.0.CO;2)
623 [0469\(1998\)055<1613:SIRRWA>2.0.CO;2](https://doi.org/10.1175/1520-0469(1998)055<1613:SIRRWA>2.0.CO;2), 1998
- 624 Williams, C. R.: Reflectivity and liquid water content vertical decomposition diagrams to
625 diagnose vertical evolution of raindrop size distributions, *J. Atmos. Oceanic Technol.*,
626 doi:10.1175/JTECH-D-15-0208.1, 2016
- 627 Williams, C. R., Beauchamp, R. M., and Chandrasekar, V.: Vertical air motions and raindrop
628 size distributions estimated from mean Doppler velocity difference from 3- and 35-GHz
629 vertically pointing radars. *IEEE Transactions on Geoscience and Remote Sensing*, 54,
630 6048–6060, [https://doi.org/10.1109/ TGRS.2016.2580526](https://doi.org/10.1109/TGRS.2016.2580526), 2016
- 631 Xu, W.: Precipitation and convective characteristics of summer deep convection over east Asia
632 observed by TRMM, *Monthly Weather Review.*, 141, 1577-1592.
633 <https://doi.org/10.1175/MWR-D-12-001>



634
 635

Table 1. Acronyms and Abbreviations Used in This Study
 Acronyms and Abbreviations

	Full Name
2DVD	Two-dimensional video disdrometer
A	Total two-way attenuation of 35-GHz VPR signals
ARSCL	Active remote sensing of clouds
ARM	Atmospheric Radiation Measurement
B	coefficients for cloud water attenuation
C	coefficients for rainfall attenuation
CLWP	Cloud liquid water path
D	Raindrop diameter
D_m	Mean mass-weighted raindrop diameter
D_{max}	Maximum diameters in the size distribution
D_{min}	Minimum diameters in the size distribution
DOE	Department of Energy
DSD	Drop size distribution
DVD	Doppler velocity difference
G	Two-way gaseous absorption
IWC	Ice water content
KAZR	Ka-band ARM zenith radar
LUT	Looking up table
LWP	Liquid water path
MB	Base of melting layer
MC3E	Mid-latitude continental convective clouds experiment
MMCR	Millimeter-wavelength cloud radar
MWR	Microwave radiometer
N_{DSD}	Number concentration
N_0	Intercept of ice particle size distribution
NOAA	National Oceanic and Atmospheric Administration
N_w	Scaling parameter in the drop size distribution
RLWP	Rain liquid water path
R_m	Layer-mean rain rate
RR	Rain rate



S_{DSD}^{λ}	Radar reflectivity-weighted velocity spectral density
v_{DSD}^{λ}	First reflectivity-weighted velocity spectrum moments represent the mean velocity
Z_{DSD}^{λ}	Raindrop terminal velocity
$\Gamma(\mathbf{x})$	Zeroth reflectivity-weighted velocity spectrum moments represent the intrinsic (non-attenuation) reflectivity factor
λ	Euler gamma function
μ	Radar wavelength
	Raindrop backscattering cross section
	Shape parameter

636

637



Table 2. Statistics (mean differences, 95% confidence interval of mean differences, RMSEs) of D_m , RR between this study (RET) and disdrometers (2DVD, RD-80) for Case A and Case B

	Mean Differences (95% confidence interval)	RMSE
Case A: D_m (RET, 2DVD) (mm)	-0.02 (-0.05, 0.01)	0.24
Case A: RR (RET, RD-80) (mm hr ⁻¹)	-0.29 (-0.40, -0.19)	0.98
Case A: RR (RET, 2DVD) (mm hr ⁻¹)	-0.31 (-0.48, -0.15)	1.45
Case B: D_m (RET, 2DVD) (mm)	-0.11 (-0.14, -0.07)	0.29
Case B: D_m (RET, 2DVD-all) (mm)	-0.09 (-0.13, -0.05)	0.34
Case B: RR (RET, RD-80) (mm hr ⁻¹)	0.34 (0.16, 0.53)	1.63
Case B: RR (RET, 2DVD) (mm hr ⁻¹)	0.17 (-0.01, 0.36)	1.61
Case B: RR (RET, 2DVD-all) (mm hr ⁻¹)	0.14 (-0.08, 0.36)	1.89

638
 639
 640
 641
 642
 643
 644
 645
 646
 647
 648
 649
 650
 651
 652
 653
 654
 655
 656

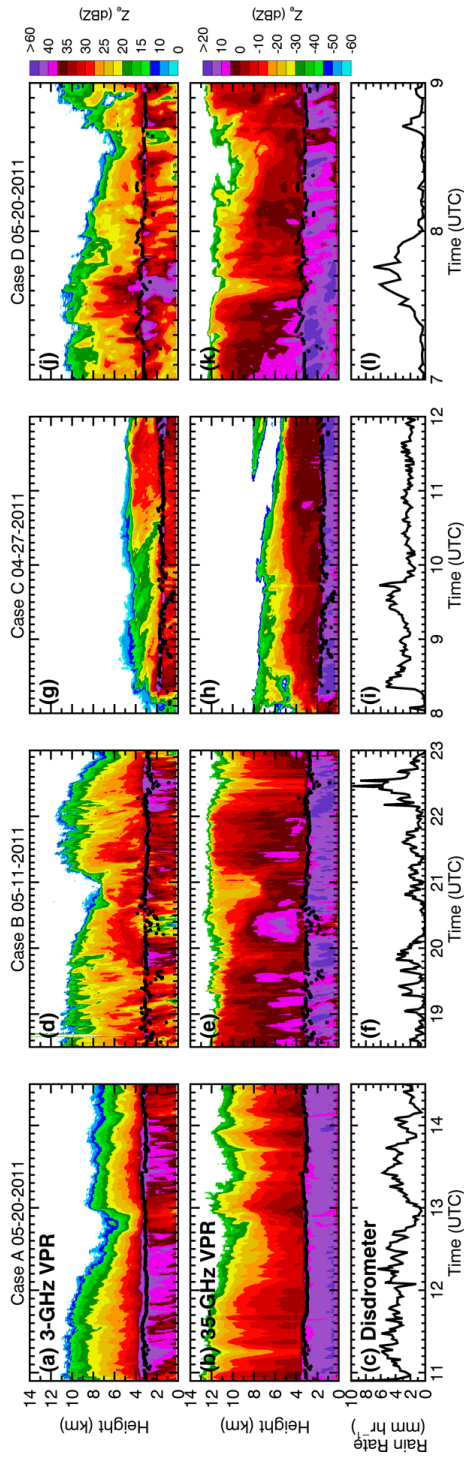


Figure 1. Time series of (a) radar reflectivity (Z_w) from NOAA 3-GHz vertical pointing radar (VPR), (b) radar reflectivity from ARM 35-GHz VPR, and (c) rain rates from RD-80 surface disdrometer measurement for Case A (20 May 2011, 11:00 – 15:30 UTC); (d)-(f) for Case B (11 May 2011, 18:30 – 23:00 UTC); (g)-(i) for Case C (27 April 2011, 8:00 – 12:00 UTC); (j)-(l) for Case D (20 May 2011, 7:00 – 9:00 UTC). Ceilometer cloud base height estimates are shown with black dots at 1-minute resolution. Note that the ranges of radar dBZ values are different in 3-GHz and 35-GHz radars.

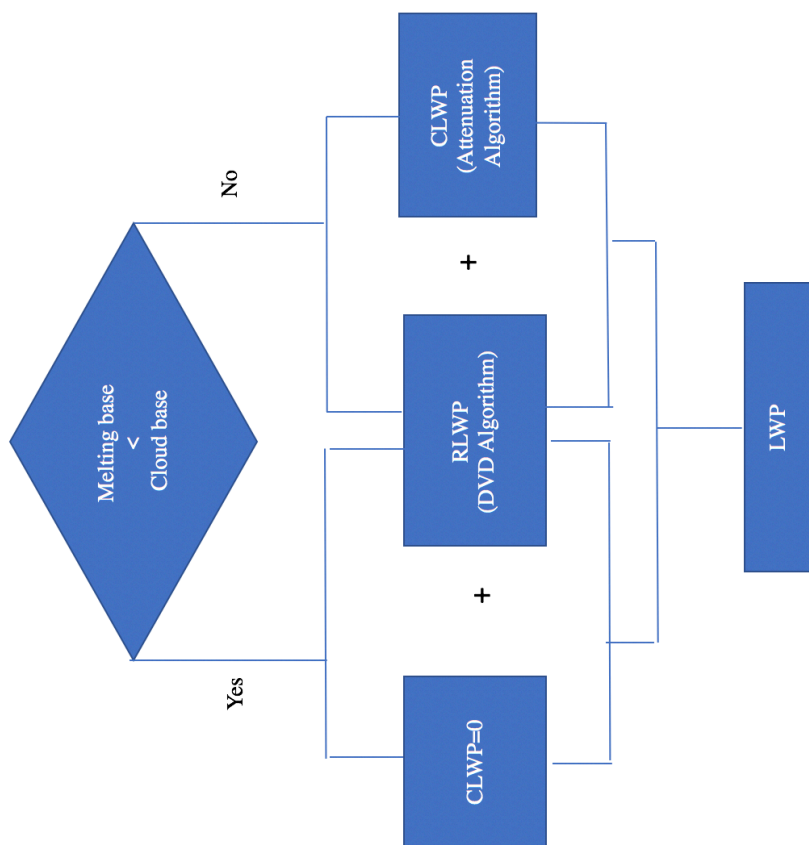


Figure 2. Algorithm flowchart to retrieve liquid water path (LWP) below melting base.

665
666

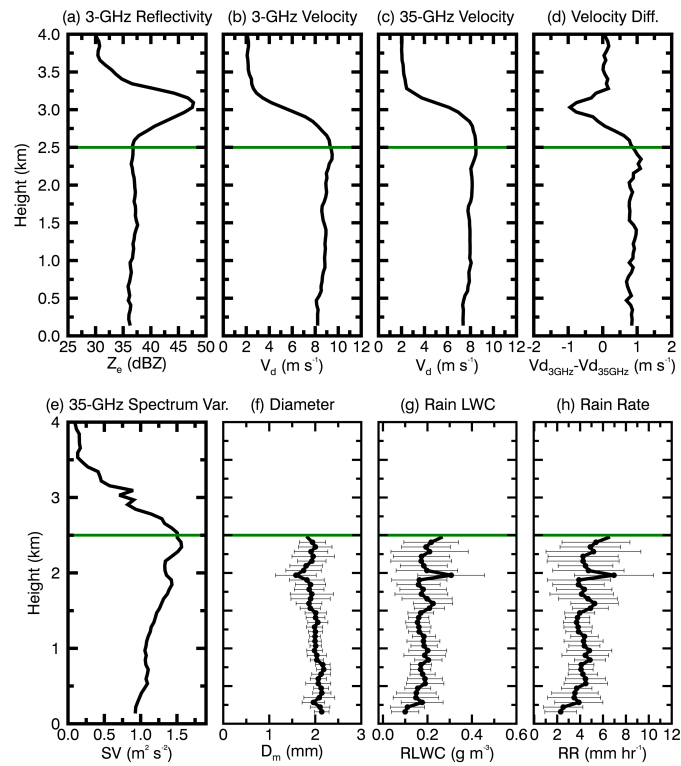
667

668

669

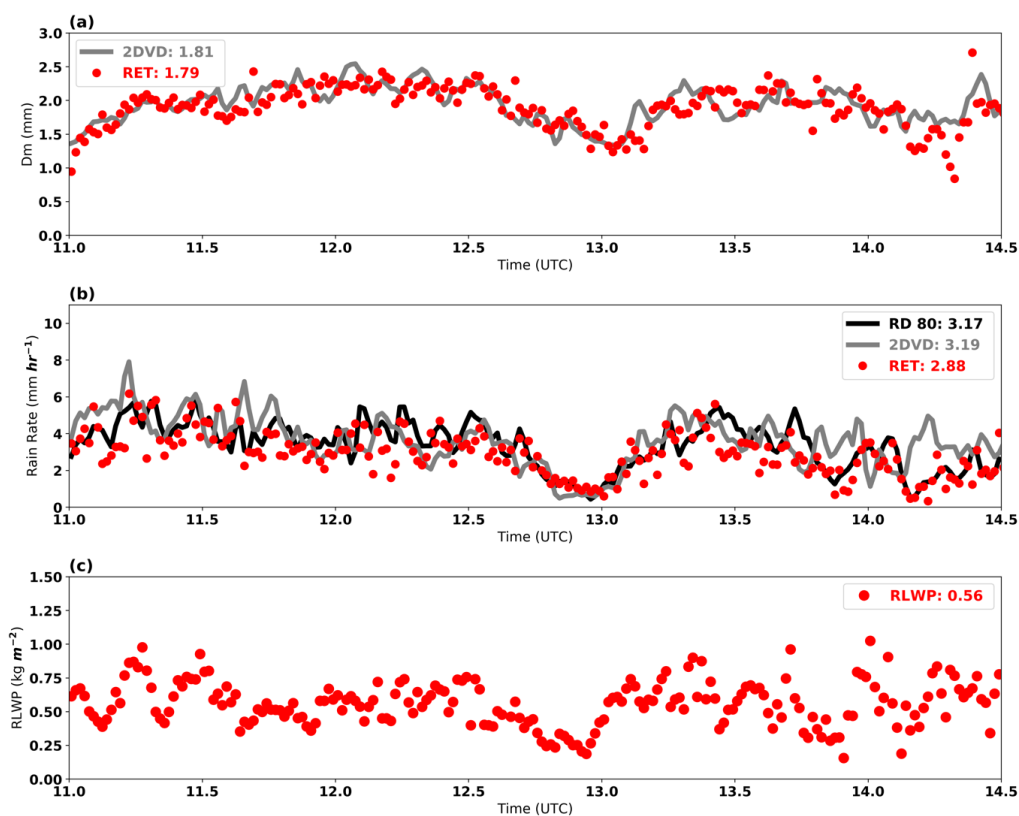


670



671

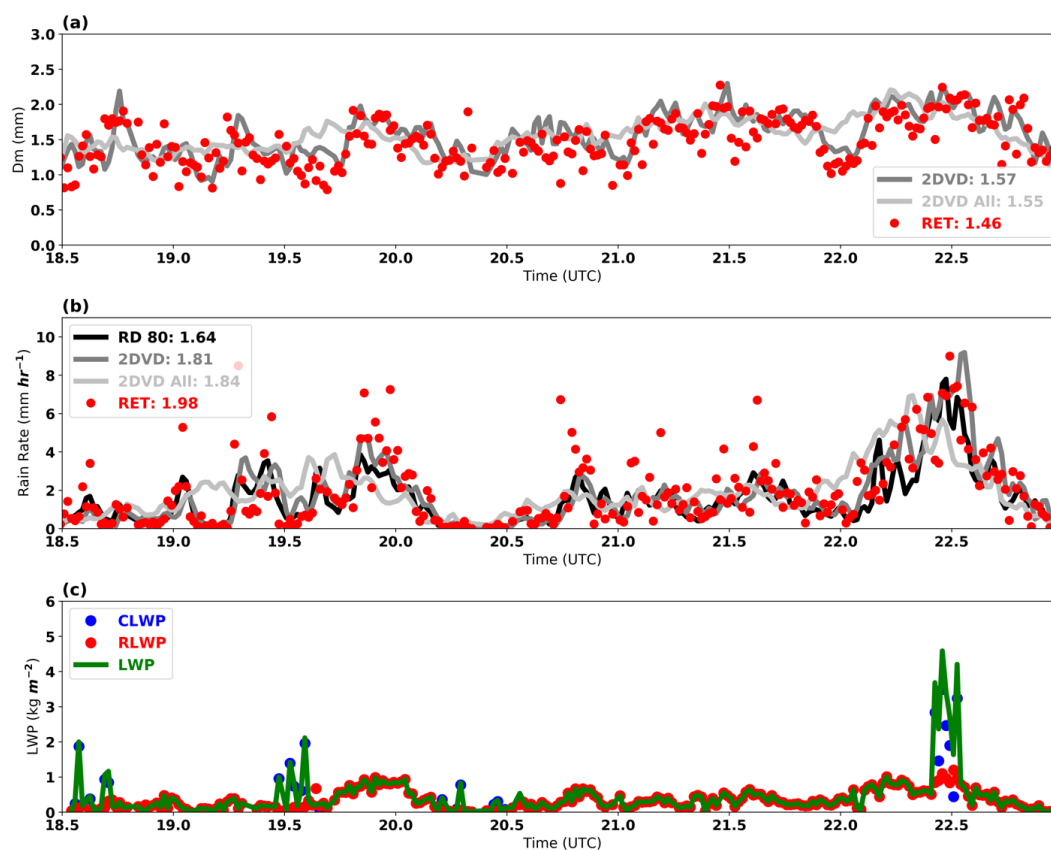
672 **Figure 3.** An example of illustrating the Doppler Velocity Differences (DVD) retrieval
 673 algorithm at 13:40 UTC on May 20, 2011. The inputs of the DVD retrieval algorithm are: (a) 3-
 674 GHz vertical pointing radar reflectivity factor (Z_e), (b) 3-GHz radar Doppler velocities (V_d), (c)
 675 35-GHz radar Doppler velocities (V_d), and (e) 35-GHz radar spectrum variances (SV). The
 676 Doppler velocity difference between 3-GHz and 35 GHz is shown in (d). The outputs of the
 677 DVD retrieval algorithm are: (f) mass-weighted mean diameter D_m , (g) rain liquid water content
 678 (RLWC), and (h) rain rate (RR). Retrieval uncertainties are shown as horizontal thin black lines.
 679



680

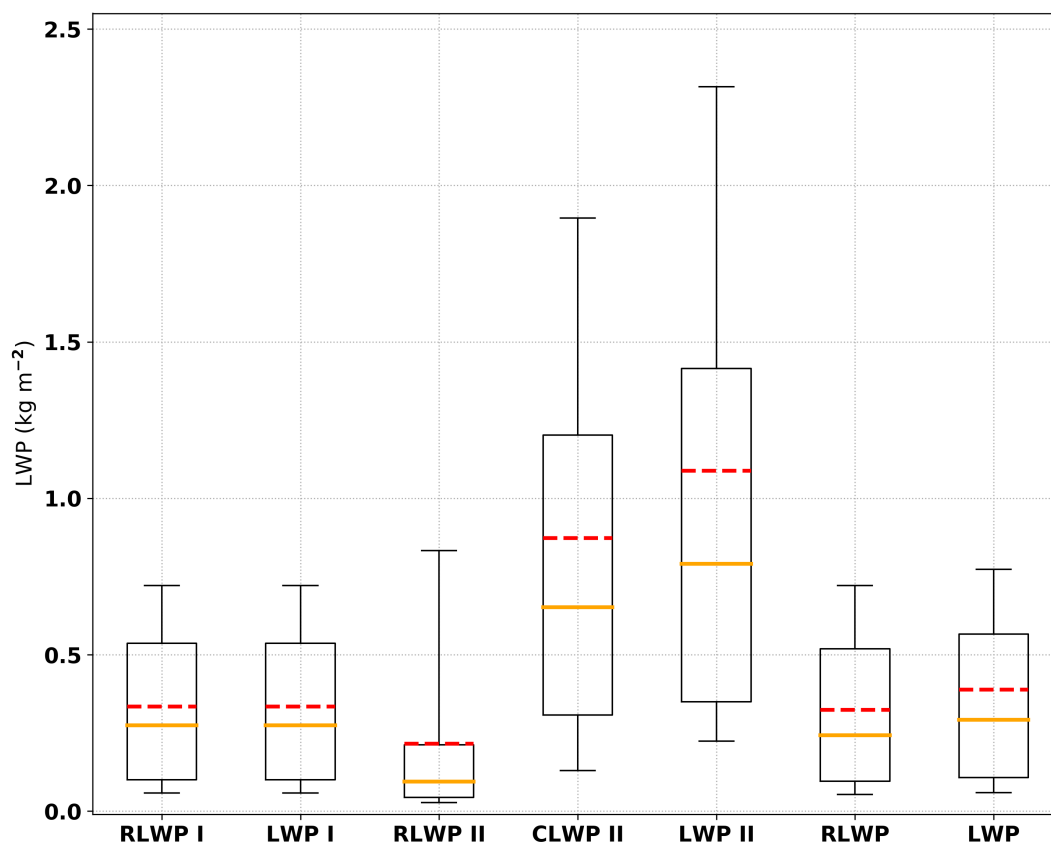
681 **Figure 4.** Time series of (a) retrieved (RET) (red dots) and 2DVD surface disdrometer estimated
 682 (grey line) D_m , (b) RET (red dots), 2DVD (grey line) and RD-80 (black line) surface disdrometer
 683 rain rate estimates, and (c) retrieved rain liquid water path (RLWP, red dots) for Case A (May 20,
 684 2011.

685



686

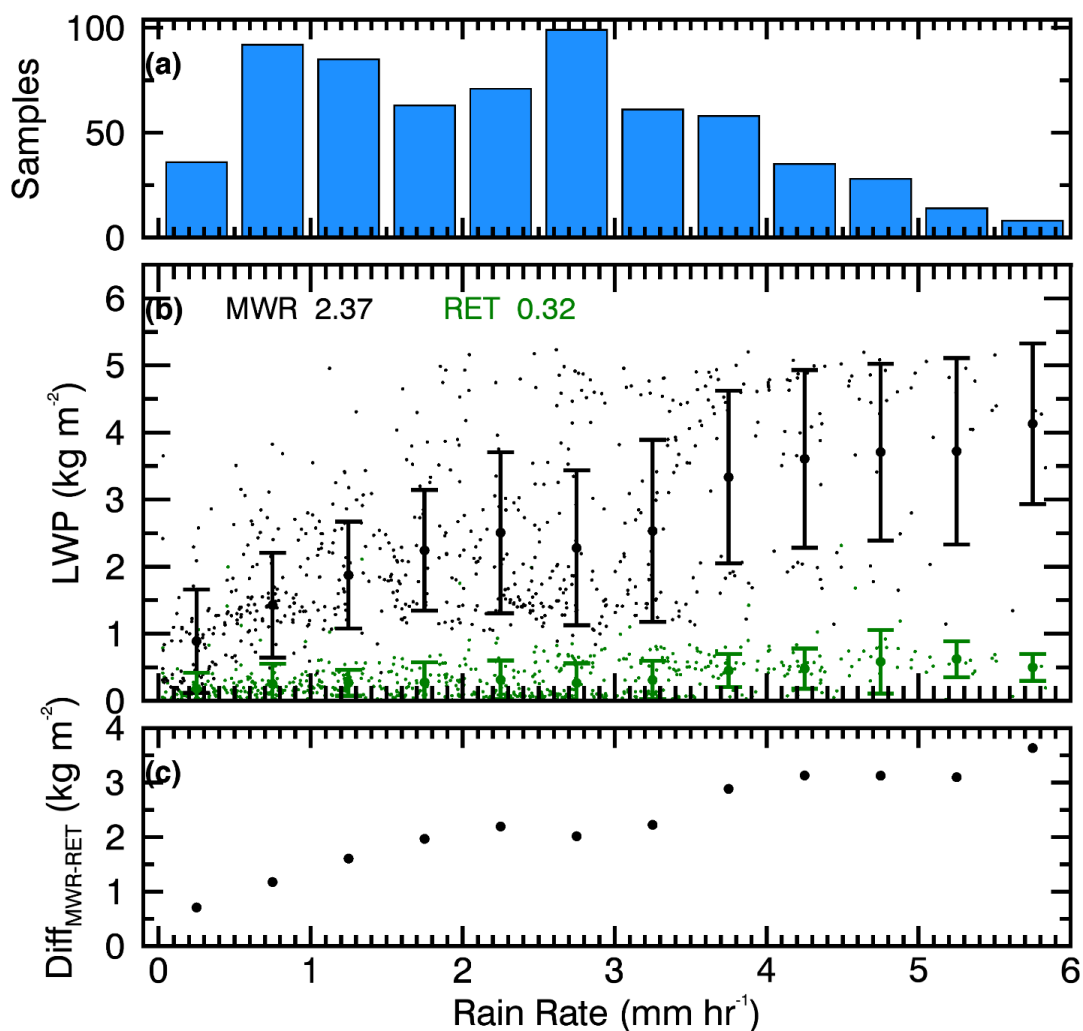
687 **Figure 5.** Time series of (a) retrieved (RET) (red dots) and 2DVD surface disdrometer estimated
688 (grey lines) D_m , (b) RET (red dots), 2DVD (grey line) and RD-80 (black line) surface
689 disdrometer rain rate estimates, and (c) rain liquid water path (RLWP, red dots), cloud liquid
690 water path (CLWP, blue dots) and liquid water path ($LWP = RLWP + CLWP$, green lines) for
691 Case B (May 11, 2011).
692



693
694 **Figure 6.** Box and whisker plots of retrieved RLWP, CLWP and LWP for situation (I), (II) and
695 all samples. The horizontal orange line within the box indicates the median, boundaries of the
696 box indicate the 25th- and 75th-percentile, and the whiskers indicate the 10th- and 90th-percentile
697 values of the results. The red dash lines indicate the mean values.
698



699



700

701 **Figure 7.** (b) Statistic comparisons between LWP retrievals from this study (RET, dots with one
702 standard deviation bars in green) and microwave radiometer (MWR, black dots with one
703 standard deviation bars in black), (a) corresponding sample numbers (blue bars) in each rain rate
704 bin (0.25 mm hr⁻¹), and (c) the LWP differences between two estimations, shown as a function of
705 rain rate for all cases.

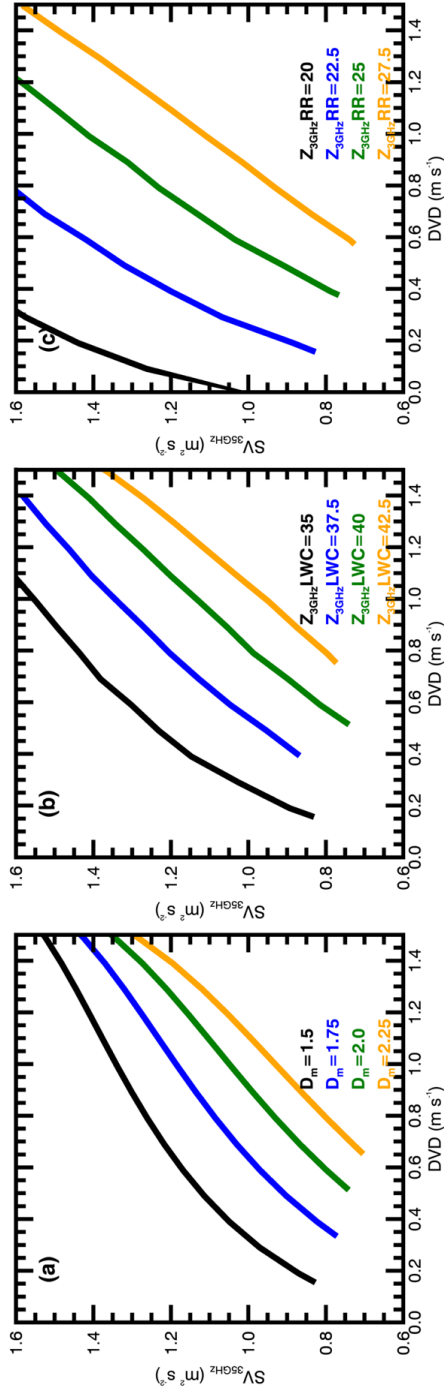


Figure A. Comparisons of (a) mass-weighted mean diameter D_m (mm), (b) parameter $Z_{3\text{GHz}} \text{LWC} = 10 \log(Z_{3\text{GHz}} \text{LWC})$ (dB), and (c) parameter $Z_{3\text{GHz}} \text{PR} = 10 \log(Z_{3\text{GHz}} \text{PR})$ (dB) calculated as functions of Doppler velocity difference (DVD) and spectrum variance at 35 GHz ($\text{SV}_{35\text{GHz}}$).

706

707

708

709

710